Acta Crystallographica Section D
Biological Crystallography
ISSN 0907-4449

A practical phasing procedure using the MAD method without the aid of XAFS measurements: successful solution in the structure determination of the outer-membrane lipoprotein carrier LolA

Kazuki Takeda,[a] Hideyuki Miyatake,[a] Naoko Yokota,[b] Shin-ichi Matsuyama,[b] Hajime Tokuda[b] and Kunio Miki[a,c]*

[a]RIKEN Harima Institute/SPring-8, Koto 1-1-1, Mikazuki-cho, Sayo-gun, Hyogo 679-5148, Japan, [b]Institute of Molecular and Cellular Biosciences, University of Tokyo, Yayoi 1-1-1, Bunkyo-ku, Tokyo 113-0032, Japan, and [c]Department of Chemistry, Graduate School of Science, Kyoto University, Sakyo-ku, Kyoto 606-8502, Japan

Correspondence e-mail: miki@kuchem.kyoto-u.ac.jp

Received 23 January 2003
Accepted 5 June 2003

A practical procedure for MAD phasing was successfully performed in the structure determination of the LolA protein, even though the XAFS data could not be measured owing to the overlap of the fluorescence spectra of the atoms that contribute significant signals for anomalous dispersion. The LolA protein, a periplasmic chaperone functioning as an outer-membrane lipoprotein carrier of the Lol system which mediates translocation of the water-insoluble outer-membrane lipoprotein across the periplasm in Gram-negative bacteria, was crystallized in two forms: orthorhombic (*I*222) and trigonal ($P3_121$ or $P3_221$). A multi-wavelength data set was collected from a platinum derivative of the orthorhombic crystals grown from a buffer solution containing zinc acetate and cacodylate (an arsenic compound), but XAFS measurements could not be performed because the energies of the fluorescence spectra of Zn atoms, As atoms and Pt atoms are in very close proximity. However, effective MAD data were collected with six wavelength data sets near the platinum absorption edge and the f' and f'' values could subsequently be estimated from the data statistics and the peak height of the dispersive and anomalous difference Patterson maps. The subsequent MAD phasing gave a high-quality initial electron-density map which was sufficient to construct a complete molecular model of the LolA protein.

1. Introduction

The Pt atom is one of the most useful heavy atoms in derivative compounds for protein crystal structure determination. Various platinum compounds such as potassium tetrachloroplatinate(II) (K_2PtCl_4), potassium hexachloroplatinate(IV) (K_2PtCl_6) and potassium tetracyanoplatinate(II) [$K_2Pt(CN)_4$] are used in the multiple isomorphous replacement with anomalous scattering (MIRAS), single isomorphous replacement with anomalous scattering (SIRAS) and multi-wavelength anomalous dispersion (MAD) methods, respectively. In order to optimize the anomalous effect, the data must be collected near the L_{III} absorption edge (11.565 keV). For the MAD method in particular, determination of the effective absorption edge from fluorescence XAFS spectra is indispensable for diffraction data collection. Three data sets are usually collected at the absorption peak having the maximum f'' value, the inflection point having the maximum $|f'|$ value and a remote point. In the course of the structure analysis of a protein, periplasmic chaperone LolA, we obtained the only one derivative, which was prepared with a platinum compound using crystals grown from a solution containing zinc ions and As atoms from the cacodylate buffer. However, the fluorescence spectrum of the Pt atom overlaps with those of the Zn and As atoms. In addition, a bent cylindrical mirror coated

with platinum was used as part of the optical component of the BL44B2 RIKEN beamline of SPring-8 where the data collection was performed (Adachi *et al.*, 2001). A platinum- or rhodium-coated mirror is widely employed in many beamlines for biological crystallography. The platinum-coated mirror absorbs X-rays at its absorption edges and the intensity of incident X-ray beams (I_0) varies drastically depending on the energy. XAFS experiments using the present crystals were difficult to perform under such conditions, although a successful MAD phasing using platinum derivatives at this beamline has been reported previously (Shimizu *et al.*, 2002). In the present case, we could not measure the exact XAFS spectrum of the platinum derivative of the LolA crystal despite many trials. Nevertheless, we were successful in estimating the appropriate energy in the phase calculation and the phases were successfully calculated to give a high-quality electron-density map.

The Lol factors, found widely in Gram-negative bacteria, are involved in the detachment of insoluble outer-membrane-specific lipoproteins from the outer leaflet of the inner membrane. Members of the Lol factors are composed of a periplasmic chaperone LolA (20 kDa; Matsuyama *et al.*, 1995), an outer-membrane receptor LolB (Matsuyama *et al.*, 1997) and the LolCDE complex belonging to the ABC transporter family (Yakushi *et al.*, 2000). The LolCDE complex recognizes the sorting signal and releases the outer-membrane lipoprotein from outside the inner membrane using ATP-hydrolysis energy (Yakushi *et al.*, 2000). The released outer-membrane lipoprotein forms a water-soluble complex with LolA. The outer-membrane lipoprotein is accepted by LolB and is subsequently incorporated into the periplasmic side of the outer membrane. Recently, some mutants at conserved residues of LolA homologues were constructed. LolA(F47E) is defective in binding lipoproteins (Miyamoto *et al.*, 2002). LolA(R43L) (Miyamoto *et al.*, 2001) can bind lipoprotein but cannot transfer the associated lipoprotein to LolB. LolA plays an essential role in the transfer reaction of outer-membrane lipoprotein in the periplasmic space. Furthermore, depletion of LolA is lethal to *Escherichia coli* (Tajima *et al.*, 1998). Although homologues of the Lol proteins have been widely found in Gram-negative bacteria, no structural information is available at present.

We report here a practical phasing procedure using the MAD method in a case where the XAFS measurements could not be performed, in the course of the structural determination of LolA from *E. coli*, using data sets from the platinum derivative.

2. Method

2.1. Expression and purification of LolA

LolA was overexpressed and purified as described previously (Matsuyama *et al.*, 1995). The plasmid (pMAN995) encoding wild-type LolA was transformed into *E. coli* strain MC4100. The cells were grown in LB medium at 310 K. Expression of the gene was induced with 0.2%(*w*/*v*) arabinose. The harvested cells were converted to spheroplasts by treatment with lysozyme and EDTA (Osborn & Munson, 1974). The spheroplasts were removed by centrifugation at 10 000*g* for 10 min and further centrifuged at 100 000*g* for 30 min to remove insoluble materials. The resulting supernatant was concentrated with Centriprep YM-10 (Millipore) and then dialyzed against 20 m*M* Tris–HCl pH 8.0. The fraction was applied to a MonoQ 10/10 column (Amersham Pharmacia Biotech) that had been equilibrated with 20 m*M* Tris–HCl pH 8.0. The column was eluted at a flow rate of 4.0 ml min^{-1} with a linear gradient of sodium chloride (0–300 m*M*). LolA was then purified with a hydroxyapatite column with a linear gradient of potassium phosphate (25–130 m*M*). LolA was eluted at ∼74 m*M* potassium phosphate and stored in a freezer at 193 K. Stored LolA was applied to the MonoQ 10/10 column again just prior to crystallization. The column was equilibrated with 20 m*M* Tris–HCl pH 8.0 and was eluted at a flow rate of 1.0 ml min^{-1} with a linear gradient of sodium chloride. The purified protein was desalted and concentrated with Centricon YM-10 (Millipore) to ∼20 mg ml^{-1} in 10 m*M* Tris–HCl buffer pH 7.4.

2.2. Crystallization

Crystallizations were carried out by the sitting-drop vapour-diffusion method using 24-well culture plates. 1.0 µl of protein solution was mixed with an equal volume of reservoir solution on a microbridge (Hampton Research). The drop was equilibrated against 200 µl reservoir solution. Two crystal forms were obtained. Orthorhombic crystals with dimensions of 0.2 × 0.15 × 0.15 mm were obtained from solution containing 15%(*w*/*v*) PEG 8000, 80 m*M* sodium cacodylate pH 6.5, 150 m*M* zinc acetate and 20%(*v*/*v*) glycerol at 277 K (Fig. 1*a*). Trigonal crystals with dimensions of 0.4 × 0.1 × 0.1 mm were obtained from solution containing 15%(*w*/*v*) PEG 1500, 20 m*M* Tris–HCl pH 8.0 and 20%(*v*/*v*) glycerol at 293 K (Fig. 1*b*).

2.3. Derivative preparation

For each crystal form, more than 50 compounds were surveyed for the preparation of heavy-atom derivatives.

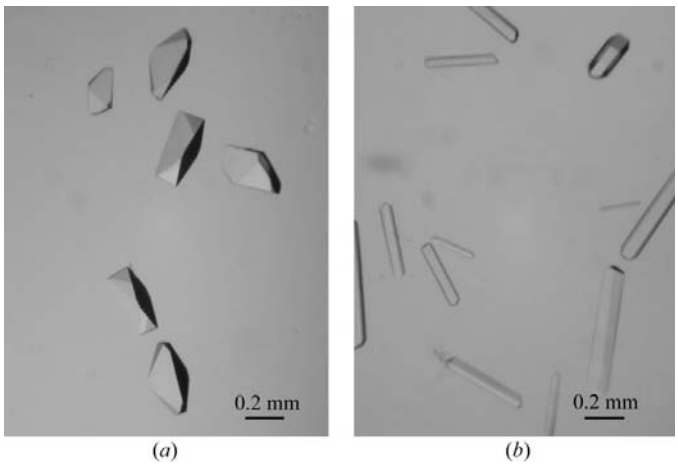

Figure 1
Crystals of LolA from *E. coli*. The scale bar indicates 0.2 mm. (*a*) Orthorhombic form (*I*222). (*b*) Trigonal form ($P3_121$ or $P3_221$).

Crystals were soaked in reservoir solutions containing 1–2 m*M* of each heavy-atom compound. Suitable derivatives were obtained for the orthorhombic crystal using three compounds having similar structures, K_2PtCl_4, K_2PtBr_4 and $K_2Pt(NO_2)_4$. The best derivative was prepared by soaking the crystals in a reservoir solution containing 2 m*M* potassium tetrabromoplatinate(II) (K_2PtBr_4) for 5 d. A back-soaking procedure was employed for 1 min. The crystals of the K_2PtBr_4 derivative were brown in colour.

2.4. X-ray data collection and analysis

For diffraction measurements at cryogenic temperature, all crystals were picked up in nylon loops (Hampton Research) and rapidly cooled with liquid ethane. The native data from the orthorhombic crystal were collected by the rotation method with oscillation angles of 1.0° at beamline BL44B2 at SPring-8 (Harima, Japan) using a MAR CCD165 detector at 90 K. The wavelength of the incident X-ray was 1.00 Å and the crystal-to-detector distance was set to 90 mm. The native data of the trigonal crystal were collected by the rotation method with oscillation angles of 2.0° at beamline BL38B1 using a ADSC Quantum 4R detector at 100 K. The wavelength of the incident X-ray was 0.998 Å and the crystal-to-detector distance was 135 mm.

Attempts were made to measure the XAFS spectrum of the platinum derivative by the fluorescence method at beamline BL44B2. An ion chamber (S-1329A, Ohyo-Koken Kogyo) and an Si-PIN photodiode detector (XR-100CR, AMPTEC) were employed for the measurement of the intensities of incident X-ray beams (I_0) and the fluorescence (I), respectively (Adachi *et al.*, 2001). The data for the MAD phasing were measured using a MAR CCD165 detector at 90 K. The crystal-to-detector distance was set to 150 mm.

All data were processed and scaled using the *HKL*2000 package (Otwinowski & Minor, 1997). Calculation of the data statistics and the Patterson maps was performed using the *CCP*4 software suite (Collaborative Computational Project, Number 4, 1994), *CNS* (Brünger *et al.*, 1998) and *XtalView* (McRee, 1999). The phases were calculated using the program *SOLVE* (Terwilliger & Berendzen, 1999) and improved by the program *RESOLVE* (Terwilliger, 2000).

3. Results and discussion

3.1. Characterization of native crystals

The orthorhombic crystals belong to the space group *I*222 (or $I2_12_12_1$), with unit-cell parameters a = 55.8, b = 75.4, c = 99.5 Å. Assuming the presence of one LolA molecule in the asymmetric unit, the Matthews coefficient V_M was calculated to be 2.57 Å^3 Da^{-1}, corresponding to a solvent content of 52.2%, which is consistent with the range previously obtained for protein crystals (Matthews, 1968). Reflection spots could be measured to 1.65 Å resolution. The trigonal crystals belong to space group $P3_121$ (or $P3_221$), with unit-cell parameters $a = b$ = 60.6, c = 79.0 Å. Assuming the presence of one LolA molecule in the asymmetric unit, the Matthews coefficient V_M was calculated to be 2.06 Å^3 Da^{-1}, corresponding to a solvent content of 40.3%, which is also a reasonable result for protein crystals (Matthews, 1968). Reflection spots extended to 1.9 Å resolution. The crystallographic data and processing statistics of both forms are listed in Table 1.

Table 1
Crystallographic data and data-collection statistics of the native data from LolA.

Values in parentheses refer to the highest resolution shell.

	Orthorhombic	Trigonal
Space group	*I*222	$P3_121$ or $P3_221$
Unit-cell parameters		
a (Å)	55.8	60.6
b (Å)	75.4	60.6
c (Å)	99.5	79.0
Resolution range (Å)	40.0–1.65 (1.71–1.65)	30.0–1.90 (1.97–1.90)
Observed reflections	363301	123965
Unique reflections	23909	13571
Redundancy	15.2 (5.6)	9.1 (7.2)
$I/\sigma(I)$	30.1 (3.1)	21.9 (5.3)
Completeness (%)	93.2 (51.6)	99.4 (99.5)
R_{sym}† (%)	4.3 (23.6)	3.9 (25.6)

† $R_{sym} = \sum_{hkl}\sum_i |I_{hkl,i} - \langle I_{hkl}\rangle| / \sum_{hkl}\sum_i I_{hkl,i}$.

3.2. Data analysis of the platinum derivative

The unit-cell parameters of the orthorhombic form of the K_2PtBr_4 derivative crystals are a = 56.5, b = 74.7, c = 98.8 Å, which differ significantly from those of the native crystals. The derivative crystals are not isomorphous with the native crystals. Only the platinum compounds successfully yielded efficient heavy-atom derivatives of the orthorhombic crystals. The cacodylate buffer containing As atoms was used as the crystallization solution and also as the soaking solution. Zinc acetate was also used in the crystallization solution. In the present case, the cacodylate and the zinc ion were not exchangeable with other reagents. The fluorescence spectrum of the As atom ($K_{\alpha1}$, 10.544 keV; $K_{\alpha2}$, 10.508 keV; $K_{\beta1}$, 11.726 keV) contained in the cacodylate compound and that of the Zn atom ($K_{\alpha1}$, 8.639 keV; $K_{\alpha2}$, 8.616 keV; $K_{\beta1}$, 9.572 keV) overlapped with that of the Pt atom ($L_{\alpha1}$, 9.442 keV; $L_{\alpha2}$, 9.362 keV; $L_{\beta1}$, 11.071 keV; $L_{\beta2}$, 11.251 keV; $L_{\gamma1}$, 12.942 keV) of the derivative crystals. Therefore, it was difficult to perform XAFS experiments using the present derivative crystals under such conditions. Consequently, the XAFS measurements were not performed and we could not determine the appropriate wavelengths for the MAD data collection. Six data sets were therefore collected from one crystal. Two data sets were collected at low-energy and high-energy remote points having small $|f'|$ values. The other four data sets were collected at four wavelengths at 0.005 Å (∼5 eV) intervals near the platinum absorption edge in order to collect a data set with a large $|f'|$ value, as wavelengths with $|f'|$ values larger than 20 e are about 0.005 Å in width. The crystal showed no significant X-ray damage during the course of data collection. The crystallographic data and processing statistics are listed in Table 2.

Table 2
Crystallographic statistics of data from the platinum derivative.

Values in parentheses refer to the highest resolution shell.

	Data set 1	Data set 2	Data set 3	Data set 4	Data set 5	Data set 6
Energy (keV)	10.781	11.550	11.555	11.560	11.566	12.399
Wavelength (Å)	1.1500	1.0735	1.0730	1.0725	1.0720	1.0000
Space group	*I*222					
Unit-cell parameters (Å)	a = 56.5, b = 74.7, c = 98.8					
Resolution range (Å)	30.0–2.50 (2.66–2.50)					
Observed reflections	43217	49596	49474	47293	48218	47649
Unique reflections	7139	7491	7497	7423	7483	7392
Redundancy	6.1 (4.1)	6.6 (5.8)	6.6 (5.8)	6.4 (5.3)	6.4 (5.6)	6.4 (5.5)
$I/\sigma(I)$	13.2 (2.3)	18.1 (3.4)	18.1 (3.5)	15.6 (2.8)	16.7 (3.2)	15.8 (2.9)
Completeness (%)	94.8 (75.2)	99.0 (94.3)	99.5 (98.5)	98.1 (89.5)	99.1 (96.6)	98.5 (92.2)
$R_{\rm sym}$† (%)	5.3 (22.8)	4.2 (17.1)	4.2 (16.1)	5.0 (20.6)	4.9 (18.1)	5.0 (20.5)
R.m.s.($\Delta F_{\rm iso}$)/r.m.s.(F)‡ (%)	[8.40]§	9.33	8.65	11.16	8.33	[8.75]§
R.m.s.($\Delta F_{\rm ano}$)/r.m.s.(F)¶ (%)	10.23	7.80	7.76	11.00	10.93	10.65
Average peak heights of $\Delta F_{\rm iso}$ Patterson maps††	[2.5]§	7.5	7.2	7.2	5.2	[1.9]§
Average peak heights of $\Delta F_{\rm ano}$ Patterson maps‡‡	4.6	4.7	5.5	7.4	8.2	7.8

† $R_{\rm sym} = \sum_{hkl}\sum_i |I_{hkl,i} - \langle I_{hkl}\rangle| / \sum_{hkl}\sum_i I_{hkl,i}$. ‡ R.m.s.($\Delta F_{\rm iso}$)/r.m.s.($F$) = $\langle \big||F| - |F_{\rm remote}|\big|^2\rangle^{1/2} / \langle |F|^2\rangle^{1/2}$. The values are averages of the values calculated using data set 1 remote data as low-energy remote data and the values calculated using data set 6 remote data as high-energy remote data. § The values of data set 1 and those of data set 6 were calculated using only data set 6 and only data set 1 as remote data, respectively. ¶ R.m.s.($\Delta F_{\rm ano}$)/r.m.s.(F) = $\langle \big||F^+| - |F^-|\big|^2\rangle^{1/2} / \langle |F|^2\rangle^{1/2}$. †† These values are averages of the values calculated using data set 1 remote data as low-energy remote data and the values calculated using data set 6 remote data as high-energy remote data. The peak heights of dispersive Patterson maps are calculated from the peak heights of three Harker sections. ‡‡ The peak heights of anomalous Patterson maps are calculated from the peak heights of three Harker sections.

Harker sections of the anomalous difference Patterson map using data set 5 at an energy of 11.566 keV (1.0720 Å) showed several strong peaks (max +9σ level) as shown in Fig. 2. The correct space group was determined to be *I*222 judging from the Patterson map. From this map, the position of the Pt atom was calculated to be (0.120, 0.423, 0.400) in Patterson space and corresponded to the position (0.060, 0.212, 0.200) or (−0.060, −0.212, −0.200) in real space.

The values of the dispersive difference ratio [r.m.s.($\Delta F_{\rm iso}$)/r.m.s.(F)] and the anomalous difference ratio [r.m.s.($\Delta F_{\rm ano}$)/r.m.s.(F)] are approximately in proportion to the $|f' - f'_{\rm remote}|$ and f'' values (Hendrickson *et al.*, 1985),

$$\begin{aligned}&\text{r.m.s.}(\Delta F_{\rm iso})/\text{r.m.s.}(F)\\ &\quad = \langle \big||F| - |F_{\rm remote}|\big|^2\rangle^{1/2} / \langle |F|^2\rangle^{1/2}\\ &\quad \propto |f' - f'_{\rm remote}|, \qquad (1)\end{aligned}$$

$$\begin{aligned}&\text{r.m.s.}(\Delta F_{\rm ano})/\text{r.m.s.}(F)\\ &\quad = \langle \big||F^+| - |F^-|\big|^2\rangle^{1/2} / \langle |F|^2\rangle^{1/2} \propto f''. \qquad (2)\end{aligned}$$

The r.m.s.($\Delta F_{\rm iso}$)/r.m.s.(F) (open circles in Fig. 3*a*) and the r.m.s. $\Delta F_{\rm ano}$/r.m.s. F (open circles in Fig. 3*b*) calculated from the six data sets are plotted against energy. The variation of the r.m.s.($\Delta F_{\rm ano}$)/r.m.s.(F) values against

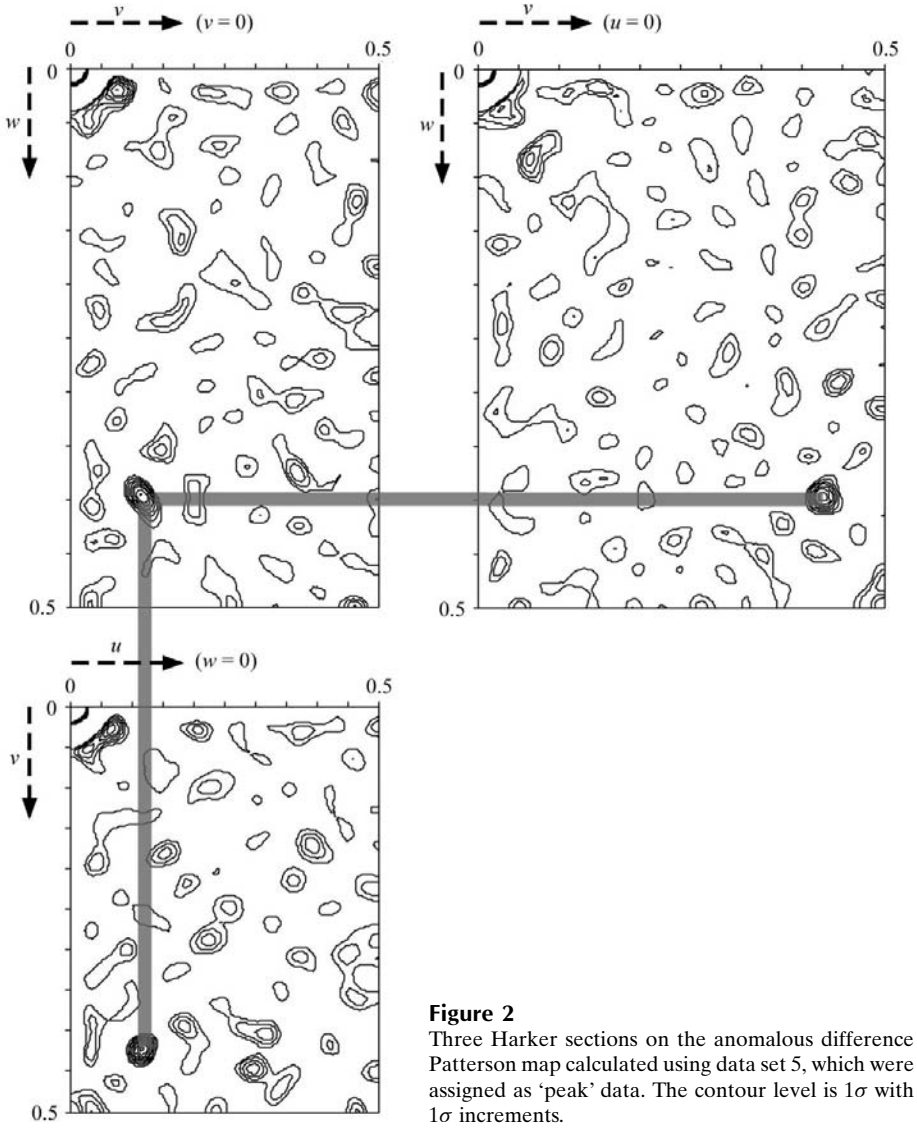

Figure 2
Three Harker sections on the anomalous difference Patterson map calculated using data set 5, which were assigned as 'peak' data. The contour level is 1σ with 1σ increments.

energy showed the same feature as that of the expected f'' value shown in Fig. 3(*d*) (solid line) and the dispersive values (open circles in Fig. 3*a*) also coincide with the expected f' values shown in Fig. 3(*c*) (solid line).

The peaks appearing in the anomalous difference Patterson map were located at the same positions where the corresponding peaks were found in the dispersive difference Patterson maps calculated using data set 1 (10.781 keV, 1.1500 Å) as the low-energy remote data or data set 6 (12.399 keV, 1.0000 Å) as the high-energy remote data. The average peak heights of the dispersive (filled circles in Fig. 3*a*) and anomalous (filled circles in Fig. 3*b*) difference Patterson maps of the six data sets were also calculated and plotted. The variation in peak heights in the anomalous Patterson maps are in good agreement with that of the expected $|f''|$ values, whereas those in the dispersive Patterson maps are not in such clear agreement.

The r.m.s.$(\Delta F_{\rm iso})$/r.m.s.(F) value, the r.m.s.$(\Delta F_{\rm ano})$/r.m.s.(F) value and the peak heights in the dispersive and anomalous difference Patterson maps are good criteria for the validity of the energy selection. Data set 4 (11.560 keV, 1.0725 Å), which has the largest r.m.s.$(\Delta F_{\rm iso})$/r.m.s.(F) value, was assigned as the 'edge' data. This data set also gave strong peaks in the dispersive difference Patterson map. Data set 5 (11.566 keV, 1.0720 Å), which is a high-energy neighbour of the edge data (data set 4), was assigned as the 'peak' data, because this data set shows a large r.m.s.$(\Delta F_{\rm ano})$/r.m.s.(F) value and a small r.m.s.$(\Delta F_{\rm iso})$/r.m.s.(F) value. The peak heights of the anomalous difference Patterson map of data set 5 are the largest among the six data sets, whereas those of the dispersive difference Patterson map are smaller than that of the 'edge' data (data set 4). These observations support the validity of the present assignment.

3.3. Phase calculations

The SAD method has been employed in recent studies on macromolecular crystallography (Brodersen *et al.*, 2000; Rice *et al.*, 2000; Dauter *et al.*, 2002). However, this method requires a higher quality of diffraction data than does the MAD method. We performed the SAD method in order to determine the initial phases, but in each case, using one wavelength data set (data sets 1 to 6), no reasonable solutions were given.

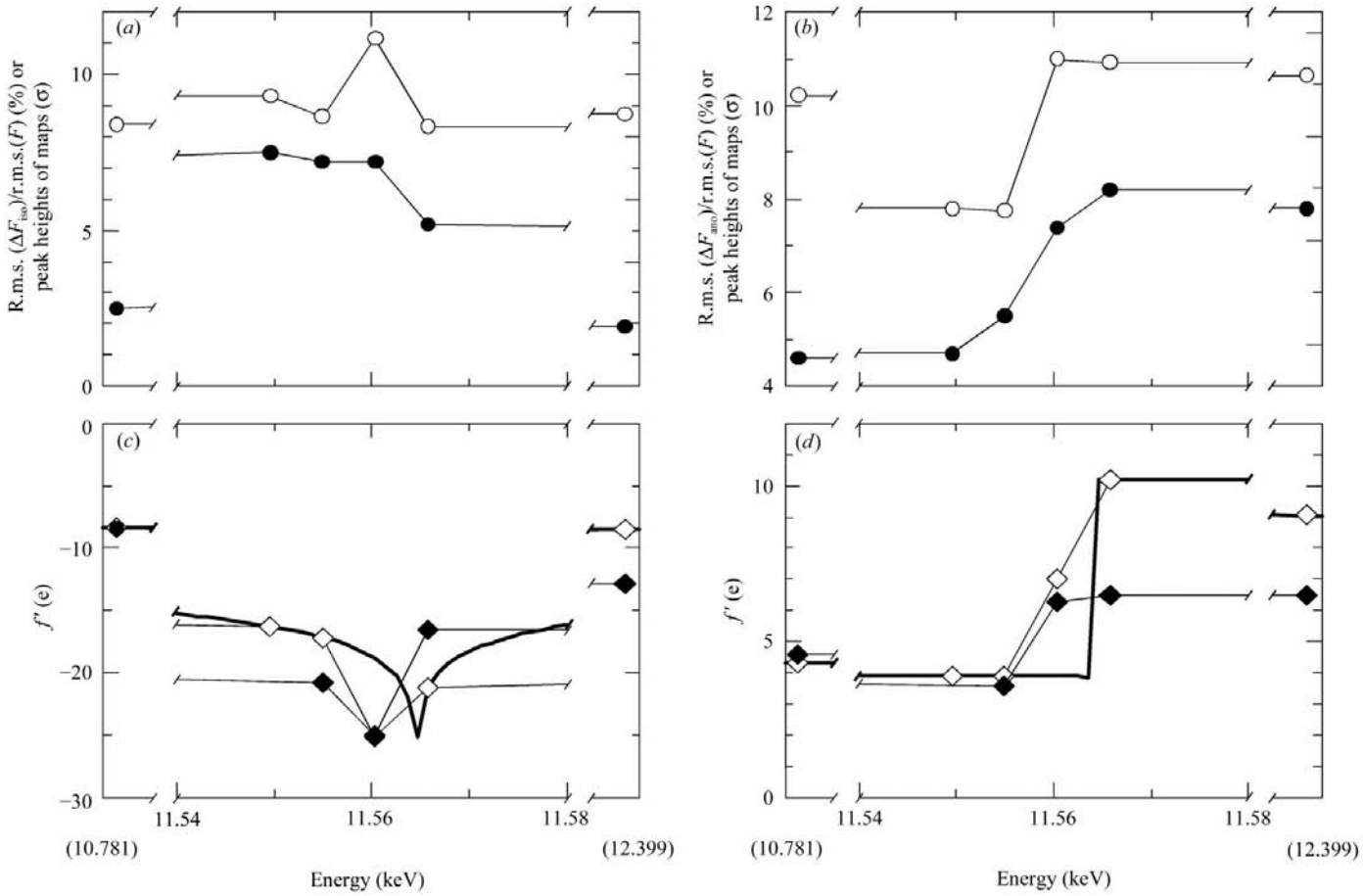

Figure 3
(*a*) Energy dependence of the dispersive difference ratio (open circles) and the peak heights of the dispersive Patterson maps (filled circles) calculated from X-ray diffraction data sets of the platinum-derivative crystals. These values are listed in Table 2. (*b*) Energy dependence of the anomalous difference ratio (open circles) and the peak heights of the anomalous Patterson maps (filled circles) calculated from X-ray diffraction data sets. These values are also listed in Table 2. (*c*) The f' values used as initial values (open diamonds) and as refined values (filled diamonds) in Phasing 5. The f' values reported in the reference (Sasaki, 1989) are plotted as solid lines. (*d*) The f'' values used as initial values (open diamonds) and as refined values (filled diamonds) in Phasing 5. The f'' values reported in the reference (Sasaki, 1989) are plotted as solid lines.

Therefore, the phases were calculated by the MAD method using three data sets (Phasing 1 in Table 3). The f' and f'' values of the peak (f' = −21.2 e, f'' = 10.2 e), edge (f' = −25.1 e, f'' = 7.0 e) and remote points (f' = −8.5 e, f'' = 9.1 e) from Sasaki (1989) were used as initial values. The Z score of the analysis was 13.83 and the overall figure of merit (FOM) was 0.44 at 2.5 Å resolution. The f' and f'' values could be reasonably refined, as listed in Table 3. Two possible positions for the Pt atoms, a major site Pt1 (0.942, 0.210, 0.195) and a minor site Pt2 (0.988, 0.261, 0.108), were found. The major site Pt1 is crystallographically equivalent to the position found in the Patterson map. The electron-density map calculated using these phases is shown in Fig. 4(*a*). The quality of the electron-density map was sufficient to identify each amino-acid residue. Another phasing procedure (Phasing 2) using data set 1 (low-energy remote data) as a 'remote' point gave a solution of the same quality (Z score = 12.63, FOM = 0.48). However, an inadequate combination of data sets (Phasing 3) gave only a poor solution (Z score = 10.21, FOM = 0.36), as shown in Fig. 4(*c*). Another phasing procedure with an inadequate data combination (Phasing 4) did not give any solutions. In addition, phase calculations using the wrong initial f' and f'' values also failed to give a sufficient solution. Therefore, the initial values of f' and f'' as well as the combination of data sets are important for the phase calculations.

Table 3
Summary of the MAD phasing.

	Initial values	Phasing 1	Phasing 2	Phasing 3	Phasing 4	Phasing 5
f'/f'' (data set 1)	−8.4/4.3	—	−12.4/3.8	—	−10.1/3.7	−8.4/4.6
f'/f'' (data set 2)	−16.3/3.9	—	—	—	—	—
f'/f'' (data set 3)	−17.2/3.9	—	—	−18.6/4.7	−20.6/2.9	20.8/3.6
f'/f'' (data set 4)	−25.1/7.0	−23.5/5.6	−27.6/5.4	—	—	−25.0/6.3
f'/f'' (data set 5)	−21.2/10.2	−12.7/6.4	−19.1/6.1	−21.1/8.9	−15.5/5.5	−16.6/6.5
f'/f'' (data set 6)	−8.5/9.1	−14.6/5.8	—	−9.1/8.0	—	−12.8/6.5
Z score	—	13.83	12.63	10.21	—	22.55
Mean FOM	—	0.44	0.48	0.36	—	0.52

The electron-density map with the best main-chain connectivity (Fig. 4*d*) was obtained when five data sets were combined (Phasing 5). Data set 2 was excluded from the phase calculation owing to limitations of the software. The Z score was 22.55 and the FOM was 0.52 at 2.5 Å resolution. The f' and f'' values were also reasonably refined in this

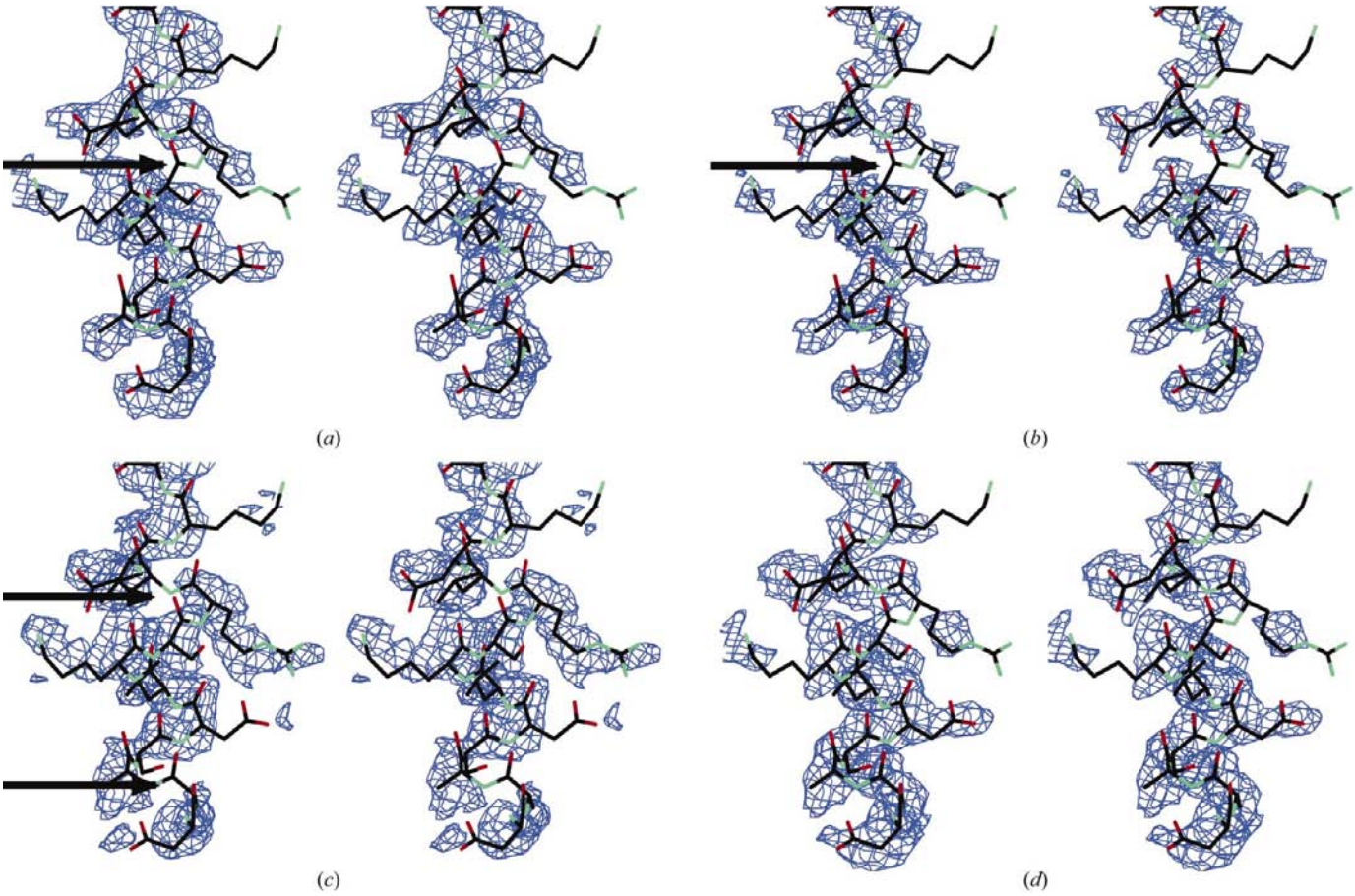

Figure 4
Electron-density map contoured at the 1σ level calculated by several MAD phasing procedures. The current structural model is indicated in stick representation. Arrows indicate disconnected parts of the main chain in the electron density. (*a*) The MAD map of Phasing 1 calculated from three data sets (4, 5 and 6). (*b*) The MAD map of Phasing 2 calculated from three data sets (1, 4 and 5). (*c*) The MAD map of Phasing 3 calculated from three data sets (3, 5 and 6). (*d*) The MAD map of Phasing 5 calculated from five data sets (1, 3, 4, 5 and 6).

phasing, as shown in Figs. 3(*c*) and 3(*d*) (filled diamonds) and Table 3. Subsequent density modification gave an overall figure of merit of 0.57. The quality of the electron-density map was sufficient for the construction of an initial molecular model (Fig. 5*a*), which enabled us to locate most of the amino-acid residues. The detailed structure of the LolA protein will be described elsewhere (Takeda *et al.*, in preparation). Two planar tetrabromoplatinate ions clearly appeared in the electron-density map (Fig. 5*b*). The major site Pt1 was located near the methionine residue (Met91), a putative ligand residue that binds to the ion. The minor site Pt2 was near another methionine residue (Met51). However, the side chains of these methionine residues were not visualized in the electron-density maps.

We could obtain high-quality electron-density maps of the LolA protein by the MAD method using several multi-wavelength data sets from one derivative, even though the XAFS measurement to determine the appropriate wavelength for the MAD data collection could not be performed owing to the proximity between the fluorescence spectrum of the Pt atom used in the derivative crystals and those of the As and Zn atoms in the buffer solution. It was demonstrated by the present work that careful analysis of the efficiency of several multiwavelength data sets in different combinations can optimize the phase calculations among the data sets. In the phase calculation, the appropriate initial values of f' and f'' could be estimated from the statistics and the peak heights of the dispersive and anomalous Patterson maps of the data sets. This procedure will be applicable to other cases where no or only a poor XAFS spectrum is available. The situation can occur when crystals contain both Se and As atoms. These two atoms also have close values of fluorescence energy but can be used in many crystallization conditions.

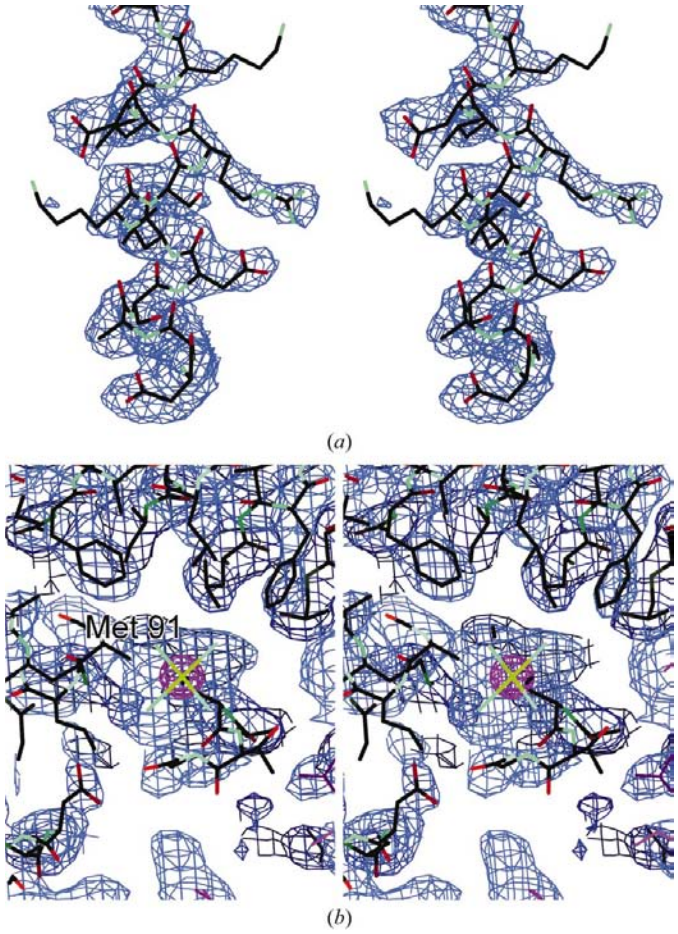

Figure 5
The modified electron-density map of Phasing 5. (*a*) The map showing the same region of Fig. 4 at the 1σ level. (*b*) The electron density of the tetrabromoplatinate ion bound to a methionine residue (Met91). Red mesh indicates the 20σ level of the anomalous difference electron-density map ($\Delta F_{\rm ano}$, $\varphi - 90^\circ$) calculated using Phasing 5 and the phases of the density-modified analysis.

We express our gratitude to Drs H. Tanida, S. Y. Park, S. Adachi and T. Hikima for their help in data collection at SPring-8. Thanks are also due to Dr N. Yasuoka for his critical reading of the manuscript and valuable comments. This work was supported by grants from the 'Research for the Future' Program of the Japan Society for the Promotion of Science and from the National Project on Protein Structural and Functional Analyses of the Ministry of Education, Culture, Sports, Science and Technology.

References

Adachi, S., Oguchi, T., Tanida, H., Park, S. Y., Shimizu, H., Miyatake, H., Kamiya, N., Shiro, Y., Inoue, Y., Ueki, T. & Iizuka, T. (2001). *Nucl. Instrum. Methods A*, **467–468**, 711–714.
Brodersen, D. E., de La Fortelle, E., Vonrhein, C., Bricogne, G., Nyborg, J. & Kjeldgaard, M. (2000). *Acta Cryst.* D**56**, 431–441.
Brünger, A. T., Adams, P. D., Clore, G. M., DeLano, W. L., Gros, P., Grosse-Kunstleve, R. W., Jiang, J. S., Kuszewski, J., Nilges, M., Pannu, N. S., Read, R. J., Rice, L. M., Simonson, T. & Warren, G. L. (1998). *Acta Cryst.* D**54**, 905–921.
Collaborative Computational Project, Number 4 (1994). *Acta Cryst.* D**50**, 760–763.
Dauter, Z., Dauter, M. & Dodson, E. (2002). *Acta Cryst.* D**58**, 494–506.
Hendrickson, W. A., Smith, J. L. & Sheriff, S. (1985). *Methods Enzymol.* **115**, 41–55.
McRee, D. E. (1999). *Practical Protein Crystallography*, 2nd ed. Academic Press, San Diego.
Matsuyama, S., Tajima, T. & Tokuda, H. (1995). *EMBO J.* **14**, 3365–3372.
Matsuyama, S., Yokota, N. & Tokuda, H. (1997). *EMBO J.* **16**, 6947–6955.
Matthews, B. W. (1968). *J. Mol. Biol.* **33**, 491–497.
Miyamoto, A., Matsuyama, S. & Tokuda, H. (2001). *Biochem. Biophys. Res. Commun.* **287**, 1125–1128.
Miyamoto, A., Matsuyama, S. & Tokuda, H. (2002). *FEBS Lett.* **528**, 193–196.
Osborn, M. J. & Munson, R. (1974). *Methods Enzymol.* **31**, 642–653.
Otwinowski, Z. & Minor, W. (1997). *Methods Enzymol.* **276**, 307–326.
Rice, L. M., Earnest, T. N. & Brünger, A. T. (2000). *Acta Cryst.* D**56**, 1413–1420.
Sasaki, S. (1989). *KEK Report 88–14*, pp. 1–136. Ibaraki, Japan: Photon Factory.
Shimizu, T., Nakatsu, T., Miyairi, K., Okuno, T. & Kato, H. (2002). *Biochemistry*, **41**, 6651–9959.
Tajima, T., Yokota, N., Matsuyama, S. & Tokuda, H. (1998). *FEBS Lett.* **439**, 51–54.
Terwilliger, T. C. (2000). *Acta Cryst.* D**56**, 965–972.
Terwilliger, T. C. & Berendzen, J. (1999). *Acta Cryst.* D**55**, 849–861.
Yakushi, T., Masuda, K., Narita, S., Matsuyama, S. & Tokuda, H. (2000). *Nature Cell Biol.* **2**, 212–218.